

The University of Texas at El Paso
Department of Mathematical Sciences
Research Reports Series

El Paso, Texas

Research Report No. 2007-08

Adaptive Multi-Mesh hp -FEM for Linear Thermoelasticity

Pavel Solin, Jakub Cervený, Lenka Dubcova



The University of Texas at El Paso
Department of Mathematical Sciences
Research Reports Series

El Paso, Texas

Research Report No. 2007-08

Adaptive Multi-Mesh hp -FEM for Linear Thermoelasticity

Pavel Solin, Jakub Cervený, Lenka Dubcova

The University of Texas at El Paso
Department of Mathematical Sciences

Pavel Solin, Jakub Cervený, Lenka Dubcova:

*Adaptive Multi-Mesh hp-FEM
for Linear Thermoelasticity*

Abstract: *We present a new adaptive hp-FEM for linear thermoelasticity where each displacement component and the temperature are approximated on different meshes which are equipped with individual energy-based adaptivity mechanisms. We demonstrate that the multi-mesh hp-FEM can capture individual behavior of every solution component more efficiently than standard hp-FEM.*

AMS subject classification: 35B50, 65N60

Keywords: Multi-mesh hp-FEM; automatic adaptivity; thermoelasticity; coupled problems

Correspondence

solin@utep.edu, jcerveny@utep.edu, ldubcova@utep.edu

Acknowledgment

The authors wish to thank to Prof. Jaroslav Kruis of the Czech Technical University in Prague for fruitful discussions related to coupled problems in engineering mechanics. This research was supported by the Czech Science Foundation (Projects No. 102/05/0629 and 102/07/0496) and by the Grant Agency of the Academy of Sciences of the Czech Republic (Project No. IAA100760702). The research of L. Dubcova was partly supported by the grant No. 48607 of the Grant Agency of the Charles University in Prague.

The University of Texas at El Paso
Department of Mathematical Sciences
500 West University, El Paso, TX 79968
Email: mathdept@math.utep.edu
URL: <http://www.math.utep.edu>
Phone: 1.915.747.5761
Fax: 1.915.747.6502

1 Introduction

Linear thermoelasticity is a standard model which describes the behavior of elastic structures subject to moderate temperature changes. The equations can be found in both classical and modern textbooks such as, e.g., [4, 6, 8, 16]. More complicated nonlinear models (not considered here) need to be employed to study the effects of large temperature changes, such as the stability of concrete or steel constructions in fire (see, e.g., [1, 5, 7, 15]). We applied the multi-mesh hp -FEM to both plane-stress and plane-strain models with similar conclusions. Due to spatial limitations, however, we only can discuss one of these models in more detail here – let us choose, for example, the latter one.

The outline of the paper is as follows: In the rest of this introductory section, we present the governing equations, boundary conditions, weak formulation, and discuss briefly the existence and uniqueness of the weak solution. In Section 2 we describe the multi-mesh hp -FEM, and in Section 3 we discuss automatic adaptivity on multiple meshes. In Section 4 we present a model problem and compare the performance of the multi-mesh hp -FEM to a (single-mesh) hp -FEM which uses the same meshes for all solution components. We also present a computation which takes into account the special coupling structure of the linear thermoelasticity system.

1.1 Plane-strain formulation of linear thermoelasticity

The plane-strain model of linear thermoelasticity inherits basic simplifying assumptions from the plane-strain model of linear elasticity,

$$\varepsilon_{33} = \varepsilon_{13} = \varepsilon_{23} = 0, \quad (1)$$

and, moreover, it assumes temperature-dependent strains in the form

$$\varepsilon_{ii} = \frac{\partial u_i}{\partial x_i} = \varepsilon_{ii,E} + \varepsilon_{ii,T} = \varepsilon_{ii,E} + \alpha(T - T_0), \quad 1 \leq i \leq 3. \quad (2)$$

Here $\varepsilon_{ii,E}$, $\varepsilon_{ii,T}$, and ε_{ii} stand for the elastic, thermal, and total strain in the x_i -direction, respectively. By u_i we denote the displacement component in the x_i -direction, α is the thermal expansion coefficient, T the temperature, and T_0 a constant temperature corresponding to a stress-free initial configuration. The material is assumed to be isotropic. Note: in the plane-strain formulation, the stress component σ_{33} is nonzero in general.

Substituting assumptions (1), (2) into the basic stress-strain relation

$$\sigma_{ij} = \frac{E}{1 + \nu} \varepsilon_{ij,E} + \frac{E\nu \sum_{k=1}^3 \varepsilon_{kk,E}}{(1 - 2\nu)(1 + \nu)} \delta_{ij}, \quad 1 \leq i, j \leq 3, \quad (3)$$

we obtain a system of equations for the stress components,

$$\left. \begin{aligned}
\sigma_{11} &= \frac{E}{(1-2\nu)(1+\nu)} [(1-\nu)\varepsilon_{11,E} + \nu(\varepsilon_{22,E} + \varepsilon_{33,E})] \\
&= \frac{E}{(1-2\nu)(1+\nu)} \left[(1-\nu) \frac{\partial u_1}{\partial x_1} + \nu \frac{\partial u_2}{\partial x_2} \right] - \frac{E\alpha(T-T_0)}{1-2\nu}, \\
\sigma_{22} &= \frac{E}{(1-2\nu)(1+\nu)} [(1-\nu)\varepsilon_{22,E} + \nu(\varepsilon_{11,E} + \varepsilon_{33,E})] \\
&= \frac{E}{(1-2\nu)(1+\nu)} \left[(1-\nu) \frac{\partial u_2}{\partial x_2} + \nu \frac{\partial u_1}{\partial x_1} \right] - \frac{E\alpha(T-T_0)}{1-2\nu}, \\
\sigma_{33} &= \frac{E}{(1-2\nu)(1+\nu)} [(1-\nu)\varepsilon_{33,E} + \nu(\varepsilon_{22,E} + \varepsilon_{11,E})], \\
&= \frac{E\nu}{(1-2\nu)(1+\nu)} \left(\frac{\partial u_1}{\partial x_1} + \frac{\partial u_2}{\partial x_2} \right) - \frac{E\alpha(T-T_0)}{1-2\nu}, \\
\sigma_{12} &= \frac{E}{2(1+\nu)} \varepsilon_{12,E} = \frac{E}{2(1+\nu)} \left(\frac{\partial u_1}{\partial x_2} + \frac{\partial u_2}{\partial x_1} \right).
\end{aligned} \right\} \quad (4)$$

Here, E and ν stand for the Young modulus and Poisson number, respectively. Substituting the stresses σ_1 , σ_2 , and σ_{12} from (4) into the equilibrium equations

$$\left. \begin{aligned}
\frac{\partial \sigma_{11}}{\partial x_1} + \frac{\partial \sigma_{12}}{\partial x_2} + f_1 &= 0, \\
\frac{\partial \sigma_{12}}{\partial x_1} + \frac{\partial \sigma_{22}}{\partial x_2} + f_2 &= 0, \\
\frac{\partial \sigma_{33}}{\partial x_3} + f_3 &= 0,
\end{aligned} \right\} \quad (5)$$

one obtains a system of second-order PDEs for the fields u_1 , u_2 and T . In (5), the only nonzero component of the volume force is $f_2 = -\rho g$. The symbols ρ , g represent the material density and the gravitational constant, respectively. If all quantities are constant in the x_3 -direction (as in our case), then the last equation in (5) is satisfied automatically.

In addition to the equilibrium equations (5), we consider the stationary heat transfer equation

$$-\nabla \cdot (a\nabla T) = 0, \quad (6)$$

where the thermal conductivity a is a nonzero constant. These equations are assumed in a bounded polygonal domain $\Omega \subset \mathbb{R}^2$.

1.2 Boundary conditions

Let the boundary $\partial\Omega$ have nonempty open subsets $\Gamma_0, \Gamma_1, \Gamma_2$ and Γ_3 such that $\Gamma_0 \cap \Gamma_1 = \emptyset$ and $\Gamma_0 \cap \Gamma_2 = \emptyset$. Equations (5), (6) are equipped with boundary conditions of the form

$$\left. \begin{aligned}
\sum_{j=1}^2 \sigma_{ij} \nu_j &= g_i^* \quad \text{on } \Gamma_0, \quad i = 1, 2, \\
u_1 &= u_1^* \quad \text{on } \Gamma_1, \\
u_2 &= u_2^* \quad \text{on } \Gamma_2, \\
T &= T^* \quad \text{on } \Gamma_3, \\
\frac{\partial T}{\partial \nu} &= T_N^* \quad \text{on } \partial\Omega \setminus \Gamma_3.
\end{aligned} \right\} \quad (7)$$

Here $g_i^*, u_i^*, T^*, T_N^* \in L^2(\partial\Omega)$, and ν is the unit outer normal vector to $\partial\Omega$. Other standard types of boundary conditions may be used as well. A model problem will be presented in Section 4.

Remark 1.1. *The linear thermoelasticity model (5), (6) has certain limitations. For example, since only derivatives of the temperature are present in the elasticity equations, the displacements and stresses only depend on spatial variation of temperature, not on its absolute values. Thus, for example, the model does not describe displacements or stresses resulting from a uniform increase of temperature. If the temperature T_0 of the stress-free initial configuration is constant, it is not taken into account by the model at all.*

1.3 Weak formulation

The solution u_1, u_2, T is sought in the form

$$u_1 = U_1 + \tilde{u}_1, \quad u_2 = U_2 + \tilde{u}_2, \quad T = \Theta + \tilde{\theta}, \quad (8)$$

where $U_1 \in V_1$, $U_2 \in V_2$, $\Theta \in V_3$. The function spaces are determined by the boundary conditions (7): $V_1 = \{\varphi \in H^1(\Omega); \varphi = 0 \text{ on } \Gamma_1\}$, $V_2 = \{\varphi \in H^1(\Omega); \varphi = 0 \text{ on } \Gamma_2\}$, $V_3 = \{\varphi \in H^1(\Omega); \varphi = 0 \text{ on } \Gamma_3\}$. The Dirichlet lifts are defined as follows: $\tilde{u}_1 \in H^1(\Omega)$ is any function satisfying $\tilde{u}_1 = u_1^*$ on Γ_1 , $\tilde{u}_2 \in H^1(\Omega)$ is such that $\tilde{u}_2 = u_2^*$ on Γ_2 , and $\tilde{\theta} \in H^1(\Omega)$ satisfies $\tilde{\theta} = \theta^*$ on Γ_3 . Equations (5), (6) are formulated in the weak sense as usual and the resulting bilinear forms can be written in a 3×3 block structure,

$$\left. \begin{aligned} a_{11}(U_1 + \tilde{u}_1, \hat{u}_1) + a_{12}(U_2 + \tilde{u}_2, \hat{u}_1) + a_{13}(\Theta + \tilde{\theta}, \hat{u}_1) &= 0 & \forall \hat{u}_1 \in V_1, \\ a_{21}(U_1 + \tilde{u}_1, \hat{u}_2) + a_{22}(U_2 + \tilde{u}_2, \hat{u}_2) + a_{23}(\Theta + \tilde{\theta}, \hat{u}_2) &= 0 & \forall \hat{u}_2 \in V_2, \\ a_{33}(\Theta + \tilde{\theta}, \hat{\theta}) &= 0 & \forall \hat{\theta} \in V_3. \end{aligned} \right\} \quad (9)$$

The derivation of the forms a_{ij} from (5), (6) is elementary and we do not include them for spatial reasons.

1.4 Problem statement

Given the boundary conditions (7) and the Dirichlet lifts $\tilde{u}_1, \tilde{u}_2, \tilde{\theta}$, find $U_1 \in V_1, U_2 \in V_2$, and $\Theta \in V_3$ satisfying (9).

Lemma 1.1. *This problem has a unique solution $(U_1, U_2, \Theta) \in V_1 \times V_2 \times V_3$. The final solution u_1, u_2, T defined by (8) does not depend on the choice of the Dirichlet lifts $\tilde{u}_1, \tilde{u}_2, \tilde{\theta}$.*

Proof: The existence and uniqueness of the solution $\Theta \in V_3$ to the third equation of (9) is obvious. Substitute Θ into the elasticity part of (9). The bounded bilinear forms a_{13}, a_{23} become bounded linear forms for \hat{u}_1 and \hat{u}_2 , respectively. Now, standard result for linear elasticity yields the existence and uniqueness of $U_1 \in V_1$ and $U_2 \in V_2$. The proof of independence of u_1, u_2, T of the Dirichlet lifts $\tilde{u}_1, \tilde{u}_2, \tilde{\theta}$ is straightforward.

2 Multi-Mesh hp -FEM

The solution components u_1, u_2, T are approximated on different meshes τ_1, τ_2 and τ_3 , respectively. For the sake of algorithmic feasibility, all meshes are defined using a common coarse *master mesh* τ_m and a finite sequence of mutually independent refinements. The master mesh τ_m is very coarse and it may not even be used for discretization purposes – it serves as the top of a tree-like structure which is utilized by the multi-mesh assembling procedure. The situation is illustrated in parts A – D of Fig. 1.

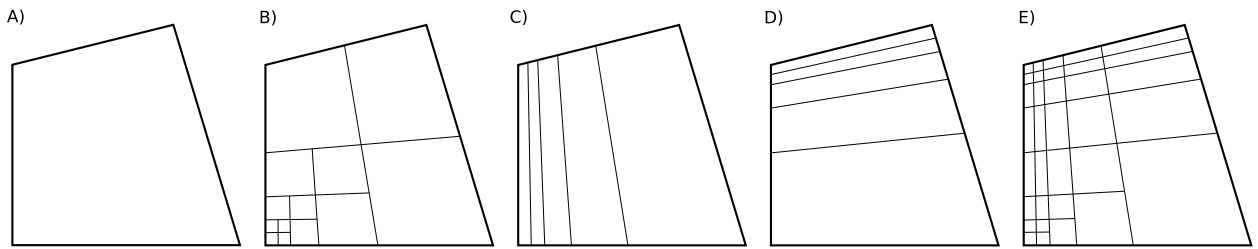


Figure 1: Example of a master mesh τ_m , meshes τ_1, τ_2, τ_3 obtained by its refinements, and the corresponding union mesh τ_u .

In part E of Fig. 1, the reader also can see the geometrical union of all meshes in the system – we call it *union mesh* and denote by τ_u .

2.1 Union mesh and the multi-mesh assembling procedure

The union mesh τ_u is never created physically in the computer memory, but its virtual elements are used by the element-by-element assembling procedure. The algorithm visits the virtual elements of τ_u , evaluates the corresponding contributions of the bilinear forms (9), and distributes the values into the stiffness matrix and right-hand side in a standard way. The multi-mesh assembling procedure is almost the same as in standard hp -FEM, up to technical details such as the transformation of integration points from the virtual elements of τ_u into the corresponding elements in the meshes τ_1, τ_2 , and τ_3 . This is illustrated in Fig. 2.

Compared to assembling over the union mesh (if the union mesh existed physically), the assembling over multiple meshes would be less efficient. This is due to an additional cost of the transformation of integration points between the virtual and physical elements, climbing the tree of meshes, etc. However, the discrete problems obtained with the multi-mesh approach typically are smaller, better conditioned, and thus faster to solve compared to a single-mesh approach. In practice, the extra expense of the multi-mesh assembling procedure is negligible compared to the savings on the discrete problem level. A comparison will be shown in Section 4.

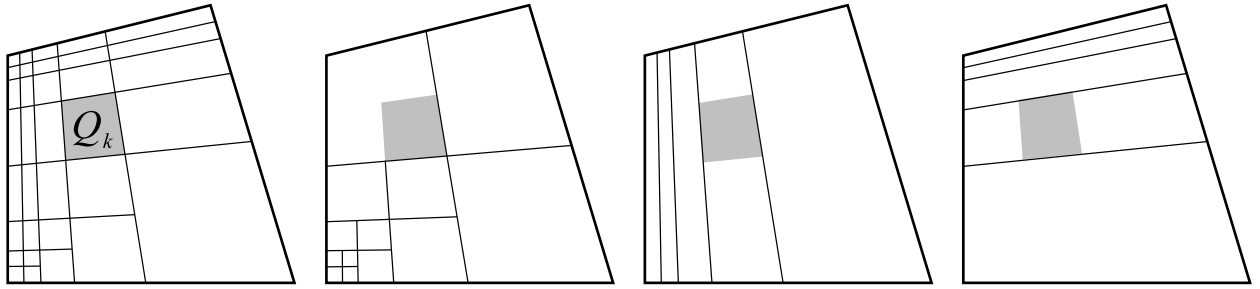


Figure 2: Virtual element Q_k of the union mesh τ_u and its counterparts in the meshes τ_1, τ_2 and τ_3 .

2.2 Integration over virtual elements

Consider a virtual element Q_k of the union mesh τ_u . In each mesh τ_i , there is exactly one element $K^{(i)}$ such that $Q_k \subset K^{(i)}$. In order to evaluate the bilinear forms a_{ij} in (9) on Q_k , we need to transform the elements $K^{(i)}$, $i = 1, 2, 3$ to the reference domain $K_q = (-1, 1)^2$. This is illustrated in Fig. 3.

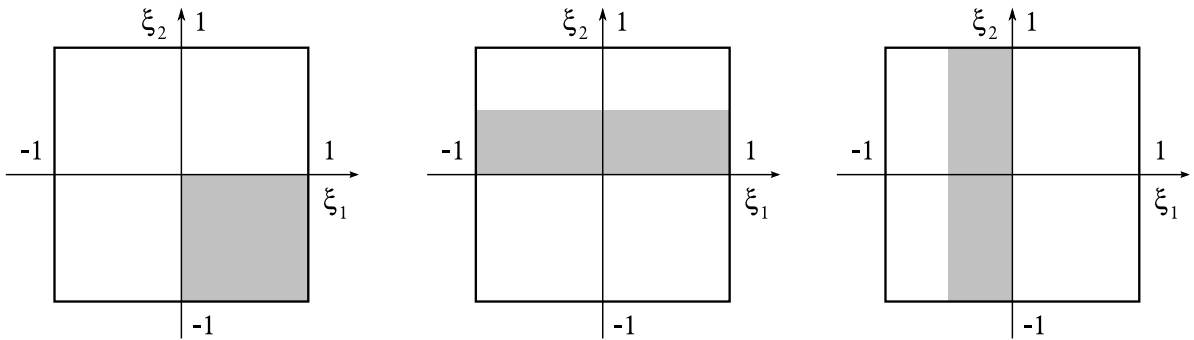


Figure 3: Elements $K^{(1)}, K^{(2)}, K^{(3)}$ of the meshes τ_1, τ_2 and τ_3 , containing Q_k , transformed to the reference domain K_q (cf. Fig. 2).

For any physical element $K = K^{(i)}$, the corresponding reference map is denoted by $\mathbf{x}_K : K_q \rightarrow K$. The reader can see that while $\mathbf{x}_K^{-1}(K) = K_q$, the virtual element $Q_k \subset K$ transforms to a subset $\mathbf{x}_K^{-1}(Q_k) \subset K_q$. However, the quadrature points and weights are designed for the entire reference domain K_q . Therefore, for each subset $\mathbf{x}_K^{-1}(Q_k)$ we need to introduce one more mapping $\mathbf{r}_K : K_q \rightarrow K_q$ such that $\mathbf{r}_K^{-1}(\mathbf{x}_K^{-1}(Q_k)) = K_q$. The situation is depicted in Fig. 4.

Note that the mapping \mathbf{r}_K is affine of the form $\mathbf{r}_K(\boldsymbol{\xi}) = \mathbf{R}_K \boldsymbol{\xi} + \mathbf{t}_K$, and therefore its Jacobi matrix is diagonal.

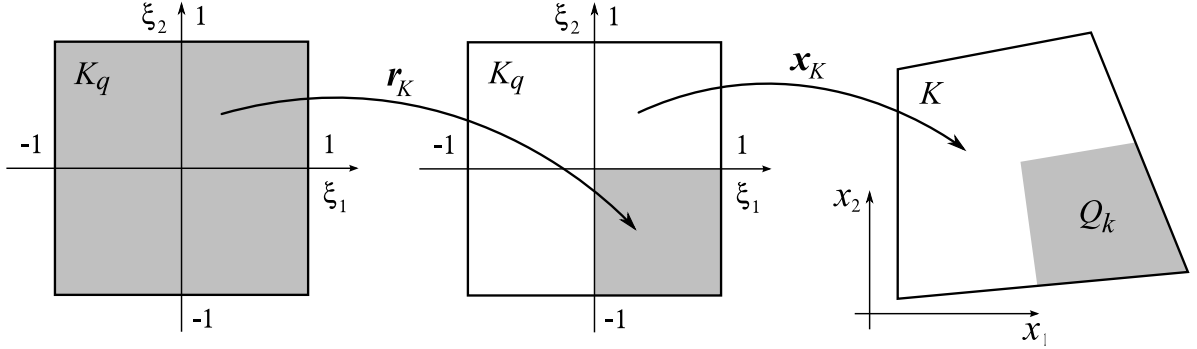


Figure 4: The mappings \mathbf{r}_K and \mathbf{x}_K .

3 Automatic Adaptivity in the Multi-Mesh hp -FEM

We assume that the reader has some knowledge of automatic adaptivity in the hp -FEM, in particular of its differences vs. automatic adaptivity in the h -FEM (see, e.g., [3, 10, 11, 13, 14] and the references therein). The exact solution $\mathbf{u} = (U_1, U_2, \Theta)$ to problem (9) is sought in a Cartesian product space $\mathbf{V} = V_1 \times V_2 \times V_3$, and the approximate solution $\mathbf{u}_{hp} = (U_{1, hp}, U_{2, hp}, \Theta_{hp})$ belongs to a subspace $\mathbf{V}_{hp} = V_{1, hp} \times V_{2, hp} \times V_{3, hp}$ of \mathbf{V} . Here, each of the piecewise-polynomial spaces $V_{i, hp}$ corresponds to the mesh τ_i in a standard way.

The approximation error $\mathbf{e}_{hp} = \mathbf{u} - \mathbf{u}_{hp} \in \mathbf{V}$ is a vector-valued function with the components $e_{1, hp} = U_1 - U_{1, hp}$, $e_{2, hp} = U_2 - U_{2, hp}$, and $e_{3, hp} = \Theta - \Theta_{hp}$. We measure the error in an energetic norm

$$\|\mathbf{e}_{hp}\|_e^2 = \sum_{i=1}^3 \|e_{i, hp}\|_{i, e}^2, \quad (10)$$

where

$$\left. \begin{aligned} \|e_{1, hp}\|_{1, e}^2 &= a_{11}(e_{1, hp}, e_{1, hp}) + a_{12}(e_{2, hp}, e_{2, hp}) + a_{13}(e_{3, hp}, e_{3, hp}), \\ \|e_{2, hp}\|_{2, e}^2 &= a_{21}(e_{1, hp}, e_{1, hp}) + a_{22}(e_{2, hp}, e_{2, hp}) + a_{23}(e_{3, hp}, e_{3, hp}), \\ \|e_{3, hp}\|_{3, e}^2 &= a_{33}(e_{3, hp}, e_{3, hp}). \end{aligned} \right\} \quad (11)$$

3.1 Estimation of error

In order to estimate the error \mathbf{e}_{hp} , we use the concept of *reference solutions* proposed by Demkowicz et al. [3]. A reference solution \mathbf{u}_{ref} is obtained by solving the problem in a larger finite element space \mathbf{V}_{ref} . This can be done in a variety of ways. For example, the space \mathbf{V}_{ref} can be constructed by refining uniformly all elements in the meshes τ_1, τ_2, τ_3 and moreover increasing the polynomial degrees of the subelements (this would be a straightfor-

ward generalization of the approach [3]). A two-grid solver can then be used to compute the reference solution \mathbf{u}_{ref} efficiently, starting from the coarse mesh solution \mathbf{u}_{hp} (see [9]).

We use a modification of this approach which is better suited for the application of sparse direct solvers: The space \mathbf{V}_{ref} is constructed by increasing the polynomial degree of all elements in the meshes τ_1, τ_2 , and τ_3 by a user-defined constant p_{inc} (default value is $p_{inc} = 3$) without spatial refinement. Then, the basis of the space \mathbf{V}_{hp} is a subset of the basis of the space \mathbf{V}_{ref} , the stiffness matrices are embedded, and the reference problem can be solved efficiently via the Schur complement method. With the solution \mathbf{u}_{ref} in hand, we compute an approximation of the error,

$$\hat{\mathbf{e}}_{hp} = \mathbf{u}_{ref} - \mathbf{u}_{hp} \approx \mathbf{e}_{hp}. \quad (12)$$

3.2 Selection of elements to be refined

Next we need to identify elements in the meshes τ_1, τ_2, τ_3 with the largest error contributions. Since we want the automatic adaptivity to take into account individual behaviors of the fields U_1, U_2 and Θ , on every mesh τ_i we only evaluate the error component $\|\hat{e}_{i, hp}\|_{i, e}$ defined in (11). In this way we obtain an error value $\hat{e}^{(i)}$ for every element $K^{(i)} \in \tau_i$. Next, the elements of all three meshes are collected in a single list L and sorted according to their error values $\hat{e}^{(i)}$ in descending order.

In every adaptivity step, we begin with the first element of the sorted list L and the refinements continue until the number of newly added degrees of freedom exceeds a user-defined constant (with default value 1000), or until the relative number of newly added degrees of freedom exceeds another user-defined constant (with default value 10%). Elements whose error values are less than 10% of the maximum error value in the list are not refined.

3.3 Element refinement

Consider an element K that was selected for refinement. The element can either be split anisotropically into two parts (in two different ways), split isotropically into four parts, or left spatially unrefined, as shown in Fig. 5.

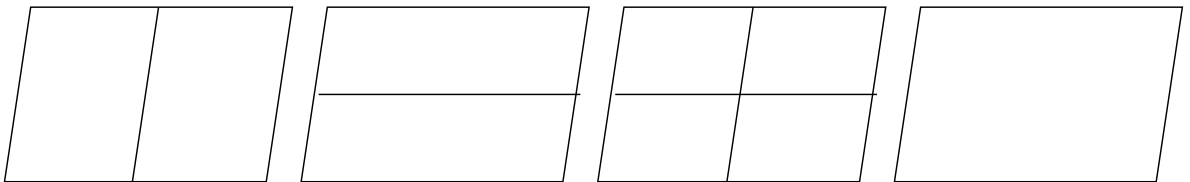


Figure 5: Four possible geometrical divisions of a quadrilateral element.

For each of these four geometrical situations we perform a variation of directional orders of approximation in the subelements, in order to create a list of refinement candidates. The user can influence this process through an integer constant $n_p \geq 0$ which limits the maximum increase of any directional polynomial degree (default value is $n_p = 1$).

In the second step, the appropriate component of the reference solution \mathbf{u}_{ref} is projected onto all refinement candidates, and a candidate with the best $\log(err)/ndof$ ratio is selected. Here, err is the element projection error and $ndof$ the number of added degrees of freedom (see [12] for details).

Due to the employment of arbitrary-level hanging nodes [12], element refinements are completely local. We do not need to take into account the situation on adjacent elements while refining an element. This eliminates unwanted refinements and simplifies the adaptivity algorithm.

4 Numerical Experiments

We consider a long hollow workpiece placed inside of a rigid form, as shown in Fig. 6. The face Γ_D is heated until its temperature reaches a value T_D . This causes a nonuniform temperature distribution in the workpiece and consequently thermoelastic deformations.

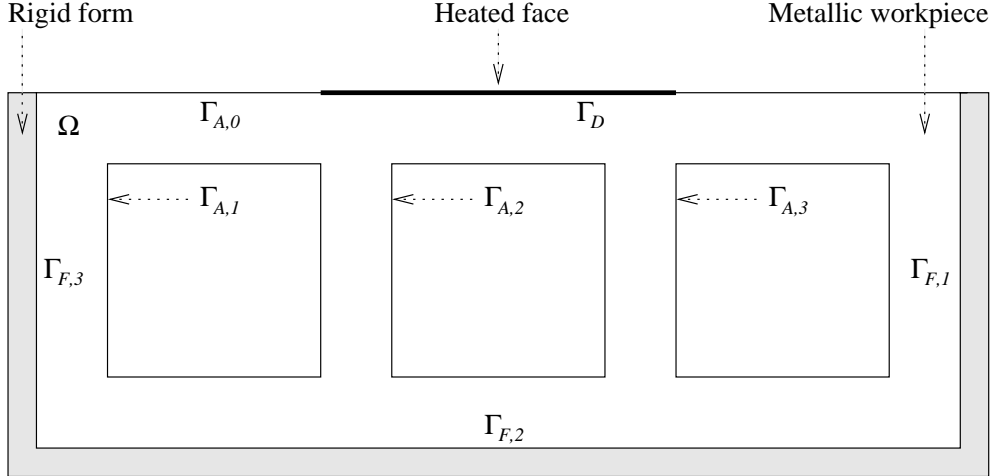


Figure 6: Transversal cross-section of the workpiece.

The transversal outer measures of the workpiece are $5L \times 13L$ and the square cavities measure $3L \times 3L$. We prescribe zero normal component of the displacement on the workpiece-

form interface Γ_F and zero external forces on the upper face of the workpiece:

$$\begin{aligned} u_1 &= 0 & \text{on } \Gamma_{F,1} \cup \Gamma_{F,3} = \Gamma_1, \\ u_2 &= 0 & \text{on } \Gamma_{F,2} = \Gamma_2, \\ \sum_{j=1}^2 \sigma_{ij} \nu_j &= 0 & \text{on } \Gamma_{A,0} \cup \Gamma_D = \Gamma_0, \quad 1 \leq i \leq 2. \end{aligned}$$

Here, ν stands for the unit outer normal vector to the boundary $\partial\Omega$. For the thermal part, we prescribe a fixed temperature T_D on the face Γ_D , and negative heat fluxes ϕ_A and ϕ_F on the workpiece-air interface Γ_A and workpiece-form interface Γ_F , respectively:

$$\begin{aligned} T &= T_D > T_0 & \text{on } \Gamma_D = \Gamma_3, \\ \frac{\partial T}{\partial \nu} &= \phi_A < 0 & \text{on } \Gamma_A, \\ \frac{\partial T}{\partial \nu} &= \phi_F < 0 & \text{on } \Gamma_F. \end{aligned}$$

In computations whose results are presented below, we used the values $L = 0.1$, $T_D = 200$, $\phi_A = -12$, $\phi_F = -20$, $\varrho = 8000$, $g = 9.81$, $a = 1.3 \cdot 10^{-5}$ (data taken from [2]).

4.1 Comparison of Multi-Mesh and Single-Mesh hp -FEM

The problem was solved using the adaptive multi-mesh hp -FEM described in Sections 2 and 3, starting from a master mesh depicted in Fig. 7.

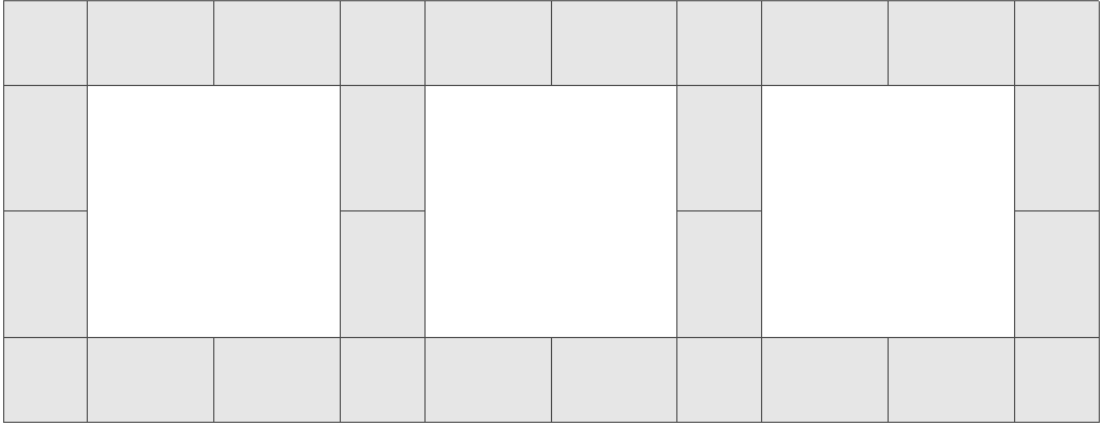


Figure 7: Master mesh for the multi-mesh hp -FEM and at the same time the starting mesh for the single-mesh hp -FEM.

Figs. 8 and 9 show the final temperature and stress distributions.

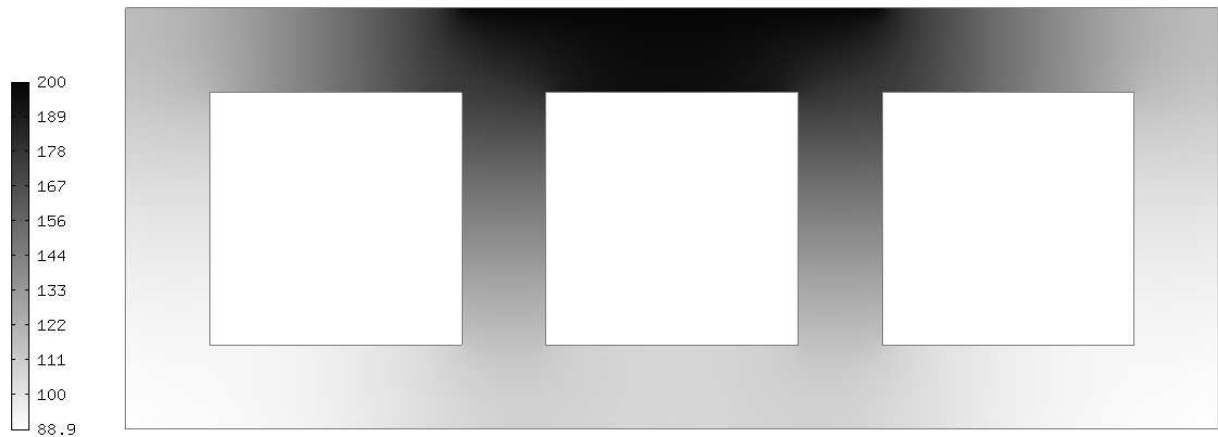


Figure 8: Final temperature distribution.

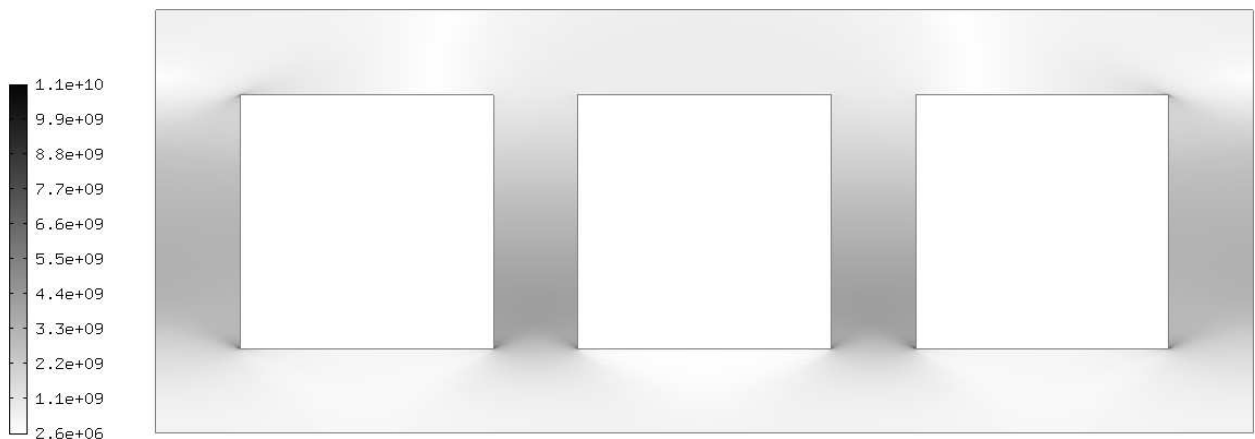


Figure 9: Final stress distribution.

For illustration, meshes corresponding to the fields u_1 , u_2 and T after 15 refinement steps are shown in Figs. 10-12, respectively. The numbers of DOF for u_1 , u_2 , T are 1309, 1602 and 205 (total of 3116). Notice that the mesh for the temperature is much coarser compared to the meshes for the displacement components.

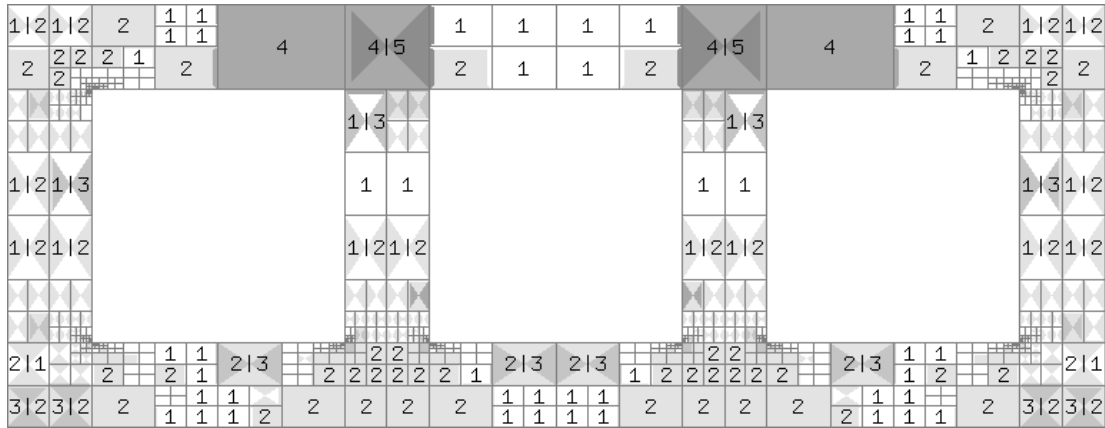


Figure 10: Multi-mesh hp -FEM: mesh for u_1 after 15 refinement steps.

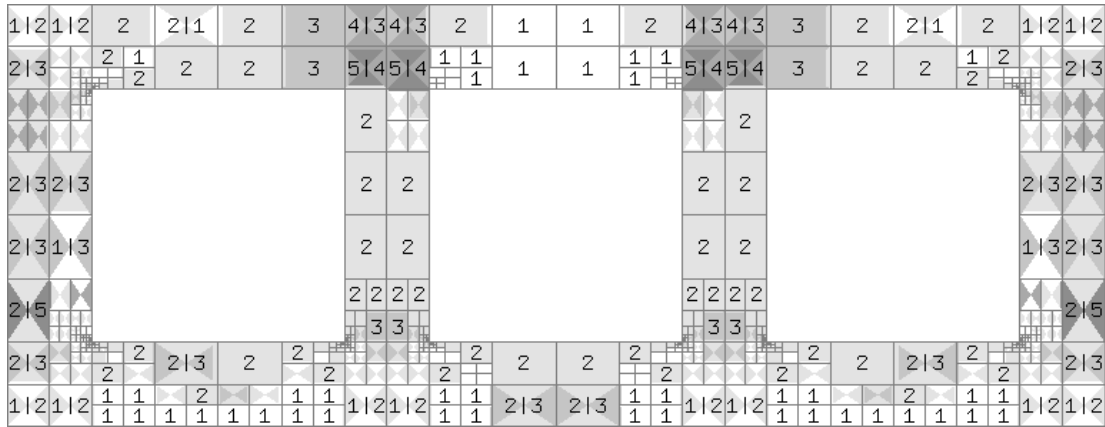


Figure 11: Multi-mesh hp -FEM: mesh for u_2 after 15 refinement steps.

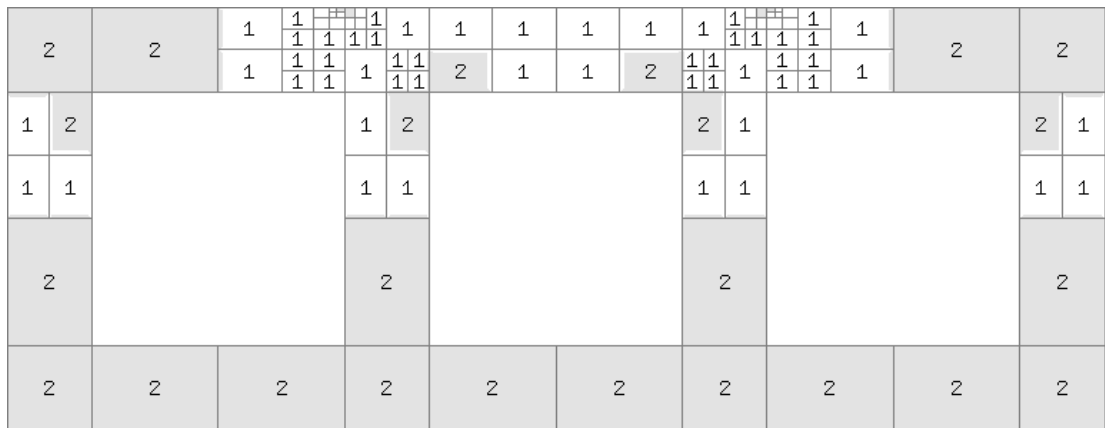


Figure 12: Multi-mesh hp -FEM: mesh for T after 15 refinement steps.

The convergence diagram in Fig. 13 shows the total error in the energy norm (10) as well as error components (11) for u_1 , u_2 and T , calculated with respect to the reference solution (12).

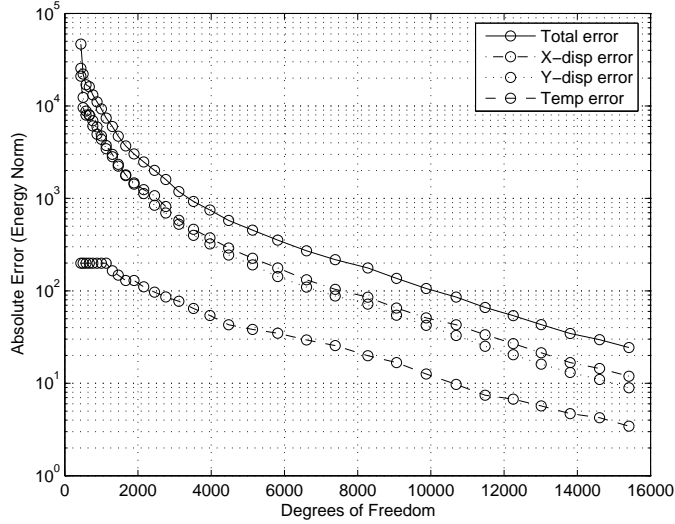


Figure 13: Convergence of the multi-mesh hp -FEM.

For comparison purposes, we also run standard adaptive hp -FEM using the same mesh for all solution components. For illustration, in Fig. 14 we show the corresponding mesh related to the same total error level as the meshes shown in Figs. 10-12. In this case, the numbers of DOF were 1542 for u_1 , 1539 for u_2 , and 1559 for T (total of 4640).

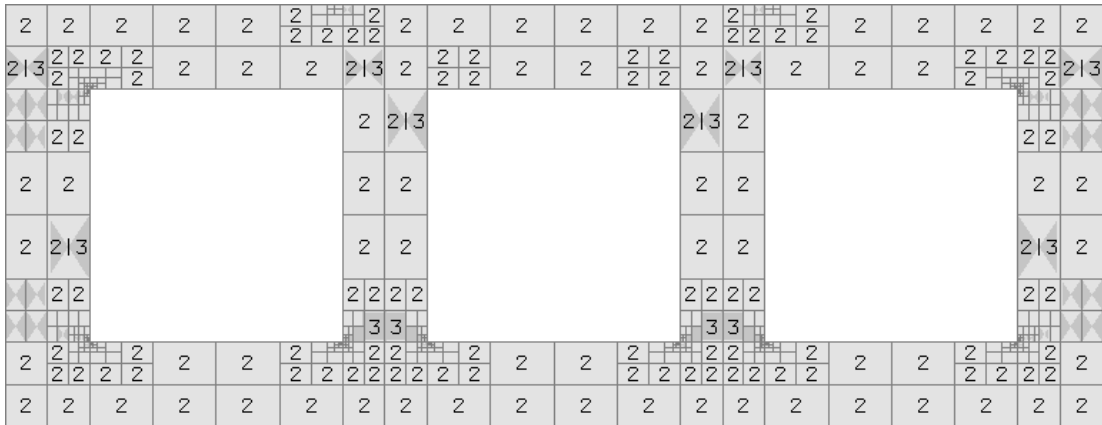


Figure 14: Single-mesh hp -FEM: mesh corresponding to the same total error as the meshes shown in Figs. 10 - 12.

The reader can see in Fig. 14 that, compared to the multi-mesh approach, the temperature T is over-resolved. The same fact follows from Fig. 15 that contains the corresponding convergence diagram.

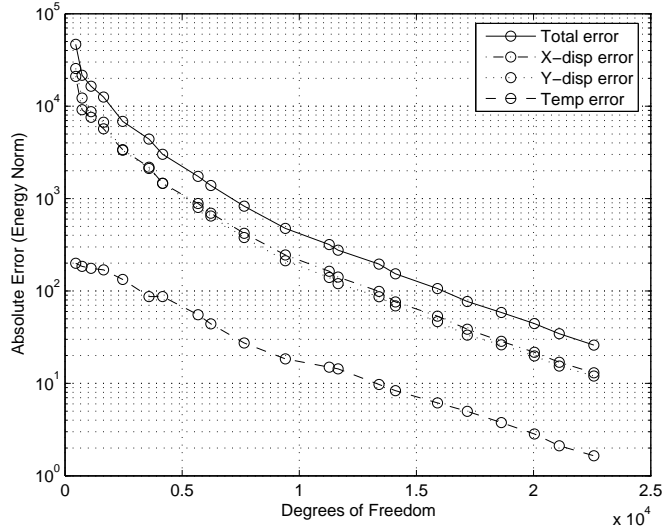


Figure 15: Convergence of the single-mesh hp -FEM.

At last let us take into account the one-way coupling between the thermal and elasticity part of the equations. First, we resolve the temperature field T accurately, starting from the master mesh shown in Fig. 7, and stopping when the error in temperature achieves a level corresponding to the end of the multi-mesh computation (with roughly 16,000 DOF for T , see Fig. 13). Then, the elasticity part of the system is solved adaptively, starting from the master mesh again, and using the temperature T as data. The multi-mesh functionality is used to deal efficiently with quantities defined on different meshes.

A convergence comparison of the three approaches mentioned above is presented in Fig. 16. Here we show the relative error values. The reader can see that the standard “single-mesh” approach was least efficient. The “economical” method which exploits the one-way coupling was most efficient both in terms of convergence speed and the CPU time of computation.

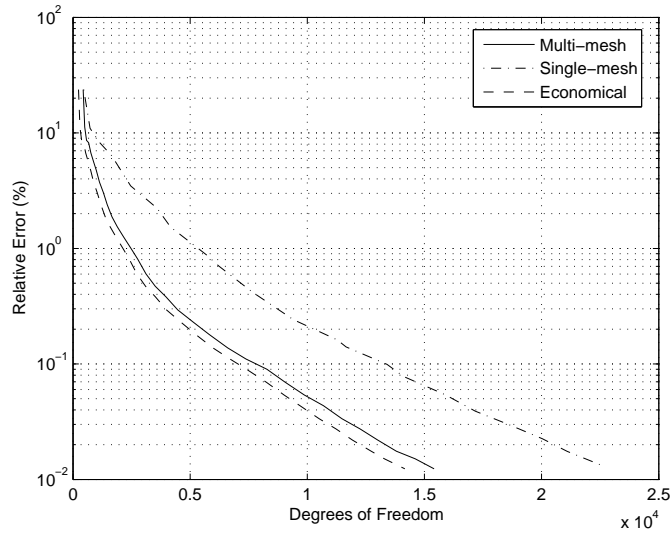


Figure 16: Convergence comparison of the multi-mesh, single-mesh, and economical approaches.

5 Conclusion and Outlook

We presented a novel adaptive higher-order finite element method for linear thermoelasticity where the solution components u_1 , u_2 and T were approximated on different meshes. These physical fields are not much different qualitatively – for example, each of them typically has singularities at re-entrant corners. In spite of that, using three meshes was more economical than approximating all of them on the same meshes. We expect that the advantage of the multi-mesh approach will become even more apparent in 3D and in more complicated coupled problems, where solution components exhibit more significant qualitative differences. Currently, we are investigating a multi-mesh hp -FEM for coupled electromagnetic-thermal problems such as microwave heating, and electromagnetic-fluid problems such as electromagnetic stirring of molten metals. We hope to report on these new results in near future.

6 Acknowledgements

The authors wish to thank to Prof. Jaroslav Krus of the Czech Technical University in Prague for fruitful discussions related to coupled problems in engineering mechanics. This research was supported by the Czech Science Foundation (Projects No. 102/05/0629 and

102/07/0496) and by the Grant Agency of the Academy of Sciences of the Czech Republic (Project No. IAA100760702). The research of L. Dubcova was partly supported by the grant No. 48607 of the Grant Agency of the Charles University in Prague.

References

- [1] Z.P. Bazant et al., *Concrete at High Temperatures, Material Properties and Mathematical Models*, Longman, Essex, 1995.
- [2] Y.A. Cengel, R.H. Turner, *Fundamentals of Thermal-Fluid Sciences*, McGraw-Hill, 2005.
- [3] L. Demkowicz, W. Rachowicz, and Ph. Devloo, A Fully Automatic hp-Adaptivity, *Journal of Scientific Computing*, 17, Nos 1-3 (2002) 127-155.
- [4] D. Iesan, A. Scalia, *Thermoelastic Deformations*, Springer, 1996.
- [5] P. C. Jain, M. N. G. Rao, Analysis of Steel Frames Under Fire Environment, *International Journal for Numerical Methods in Engineering* 19 (2005) 1467 - 1478.
- [6] A.M. Kosevich, E M Lifshitz, L D Landau, L. P. Pitaevskii, *Theory of Elasticity. Third Edition*, Butterworth-Heinemann, 1986.
- [7] T.T. Lie, R.J. Irwin, Method to Calculate the Fire Resistance of Reinforced Concrete Columns with Rectangular Cross Section, *ACI Structural Journal* 90 (1993) 52 - 60.
- [8] J.E. Marsden, T.J.R. Hughes, *Mathematical Foundations of Elasticity*, Dover Publications, 1994.
- [9] D. Pardo, L. Demkowicz: Integration of hp-Adaptivity and Multigrid. I. A Two Grid Solver for hp Finite Elements, TICAM Report 02-33, 2002.
- [10] W. Rachowicz, D. Pardo, and L. Demkowicz, Fully Automatic hp-Adaptivity in Three Dimensions, ICES Report 04-22, 2004.
- [11] C. Schwab, M. Suri, *The p and hp Versions of the Finite Element Method for Problems with Boundary Layers*, *Mathematics Computation* 65 (1996) 103 - 1429.
- [12] P. Solin, J. Cerveny, I. Dolezel: Arbitrary-Level Hanging Nodes and Automatic Adaptivity in the hp-FEM, MATCOM, in press, doi:10.1016/j. matcom.2007.02.011.
- [13] P. Solin, L. Demkowicz, Goal-Oriented hp-Adaptivity for Elliptic Problems, *Comput. Methods Appl. Mech. Engrg.* 193 (2004) 449-468.

- [14] P. Solin, K. Segeth, I. Doležel, *Higher-Order Finite Element Methods*, Chapman & Hall/CRC, Boca Raton, 2004.
- [15] M.J. Terro, Numerical Modelling of the Behaviour of Concrete Structures in Fire, *ACI Structural Journal* 95 (1998) 183 - 193.
- [16] S. Timoshenko, *Theory of Elasticity*, McGraw-Hill, 1970.